COMMUNICATIONS CHEMISTRY

ARTICLE

https://doi.org/10.1038/s42004-019-0233-1 OPEN

P band intermediate state (PBIS) tailors photoluminescence emission at confined nanoscale interface

Taiqun Yang [1], Bingqian Shan[1], Fang Huang[2*], Songqiu Yang [3], Bo Peng[1], Enhui Yuan[1], Peng Wu[1*] & Kun Zhang [1*]

The availability of a range of excited states has endowed low dimensional quantum nanostructures with interesting luminescence properties. However, the origin of photoluminescence emission is still not fully understood, which has limited its practical application. Here we judiciously manipulate the delicate surface ligand interactions at the nanoscale interface of a single metal nanocluster, the superlattice, and mesoporous materials. The resulting interplay of various noncovalent interactions leads to a precise modulation of emission colors and quantum yield. A new p-band state, resulting from the strong overlapping of p orbitals of the heteroatoms (O, N, and S) bearing on the targeting ligands though space interactions, is identified as a dark state to activate the triplet state of the surface aggregated chromophores. The UV-Visible spectra calculated by time-dependent density functional theory (TD-DFT) are in quantitative agreement with the experimental adsorption spectra. The energy level of the p-band center is very sensitive to the local proximity ligand chromophores at heterogeneous interfaces.

[1] Shanghai Key Laboratory of Green Chemistry and Chemical Processes, School of Chemistry and Molecular Engineering, East China Normal University, No. 3663, North Zhongshan Road, 200062 Shanghai, P.R. China. [2] College of Chemistry, Chemical Engineering and Materials Science, Shandong Normal University, 250014 Jinan, P.R. China. [3] State Key Laboratory of Molecular Reaction Dynamics, Dalian Institute of Chemical Physics, Chinese Academy of Sciences, 116023 Dalian, P. R. China. *email: fanghuang@sdnu.edu.cn; pwu@chem.ecnu.edu.cn; kzhang@chem.ecnu.edu.cn

The availability of a range of excited states has enriched low-dimensional quantum nanostructures with interesting luminescence properties, including noble metal nanoclusters (NCs), semiconductor quantum nanostructures (black phosphorus nanosheet and transition metal dichalcogenides as typical examples), and carbon (or graphene) quantum dots[1–4]. Among all of these, metal NCs with a precise number of metal atoms and ligands possess an exciting interface, which has the potential to elucidate fundamental electron exchange and energy transfer pathways driving nanoscale phenomena[5–7]. Even though the nanocluster-centered free-electron model based on quantum confinement mechanism have been studied for over a decade, the elucidation on the origin of the optoelectronic properties of metal NCs is diverse and contradictory, at every point inviting inquiry and debate[1,8–16]. Previously, we provided key evidence for the first time that the self-assembling of surface protecting ligands on the metal core played a paramount role to tune the optoelectronic properties of noble metal NCs[12,13,17]. Recently, the ubiquitious role of ligand assembly, domain-mediated and with incredible diversity and specificity in biological processes was also observed, including growth control, signal transduction, cell adhesion, hemostasis, and lipid metabolism[18–22]. However, the basic chemical principle hidden behind the abnormal optical and biochemical phenomena remains highly elusive[5,9–14].

Here we use the most extensively studied aqueous glutathione (GSH)-coated Au NCs as a model system. By manipulating the delicate surface ligand interactions on the individual metal nanocluster, the self-assembled metal NCs in superlattice, and the confined silica nanopores, we successfully achieve the precise control of emission colors and the systematic tuning of PL quantum yields and lifetimes. Thereby, we carefully control the solvophobicity and solvophilcity of the ligands. Our results isolate the role of the local patterning or spatial arrangement of surface ligands in the PL emissions of metal NCs. On the basis of the combined characterizations of the steady-state absorption, excitation, and time-resolved PL spectroscopy, we identify that the interfacial p-band intermediate state (PBIS) stems from the overlapping of p orbitals of the paired or more adjacent heteroatoms (O and S) bearing on the protected ligands on the metal core. Through-space conjugation within the ligand assembly domain provides effective emission luminogens. This can be considered as a dark state to activate the triplet state of the surface aggregated chromophores by enhancing intersystem crossing.

Results

Solvent-induced ligand-dependent emission of individual Au NCs. Water-soluble Au NCs were successfully prepared using glutathione (GSH) with double organic functions of carbonyl and thiol as the capping-ligand[5]. Using the longer chain 1-dodecanethiol (DT) with a single thiol group as a ligand-exchange agent, the oil-soluble Au NCs with identical size were prepared by a simple surface ligand exchange reaction (Supplementary Fig. 1). The water-soluble and oil-soluble switchable Au NCs were denoted as Au NCs@GSH and Au NCs@DT, respectively. The infrared adsorption spectrum (IR) and thermal gravimetric (TG) analyses showed strong evidences that the primitive GSH ligands could be completely replaced by 1-dodecanethiol molecules (Supplementary Figs. 2 and 3), and the kinetics of the ligand exchange reaction followed a first-order reaction with a reaction rate constant of 5.78 min^{-1} in a mixture solution of ethanol and water (Supplementary Fig. 4). It is worthy to note that the ligand exchange reaction did not occur in pure ethanol solution, indicating the presence of a stable ligand assembly on the metal core (Supplementary Fig. 5). MALDI-TOF mass spectrum shows that the composition of as-synthesized Au NCs@GSH is the same as reported by Tsukuda and colleagues[23] and Xie and colleagues[5] ($Au_{9-12}SG_{10-12}$). After ligand exchange, four peaks are observed at ~2.6, 3.0, 3.4, 3.9 kDa which are a good match for the $Au_{7-10}DT_{6-9}$ species. These results indicate that the Au core was maintained during the ligand exchange process, as shown in Supplementary Figs. 6 and 7.

The ligand exchanged Au NCs exhibit a strong solvophobicity- and solvophilicity-dependent photoluminescence emission features in Fig. 1. The water-soluble Au NCs@GSH was not luminescent in pure water (Fig. 1a and top row of inset in Fig. 1b). In contrast, hydrophobic-DT-exchanged Au NCs showed a strong red emission at 620 nm in water solution (Fig. 1c and bottom row of inset in Fig. 1b). When water-soluble Au NCs@GSH were dispersed into the mixed solution of water and ethanol, with the increase of the volume fraction of ethanol in the solvent ($R_{EtOH} = Vol_{EtOH} / Vol_{EtOH+H2O}$), a broad-peak emission at ~ 560 nm with an FWHM around 200 nm was observed, and the emission was intensified and blue-shifted, especially at a critical ethanol concentration of $R_{EtOH} \geq 75\%$ (Fig. 1a), consistent with the results reported by Xie and his coworkers[5]. Using Lorentzian functions, this broad emission peak can be decomposed into two peaks located at 550 and 620 nm (Supplementary Fig. 8a), and a close inspection of photoluminescence spectra revealed that the strength of emission growth at 550 nm was far greater than that of 620 nm (Supplementary Fig. 8b), indicating the presence of dual-channel decay pathways. The observations of two distinguished lifetimes in several and a dozen microseconds by the dynamic fitting of time-resolved PL spectroscopy, for oil-soluble Au NCs@DT and water-soluble Au NCs@GSH, respectively (Fig. 1d and Supplementary Table 1), further support the dual-channel radiation decay. Even the DT-exchanged Au NCs exhibited a similar solvent-induced emission (SIE) enhancing effect, only a single emission peak at 620 nm being observed free of 550 nm PL emission (Fig. 1c), demonstrating a single-channel PL radiation decay.

The absorption and excitation spectra of two types of Au NCs both before and after ligand exchange bore a strong resemblance in the UV region within 260− 400 nm, except for a wavelength shift (Fig. 1a−c and Supplementary Fig. 9). Three distinct absorption bands at ca. 300, 340, and 380 nm are observed for both water-soluble and oil-soluble Au NCs, consistent with our previously reported results[13]. With the increase of R_{EtOH} and R_{H2O}, the adsorption intensity of both samples was intensified (Fig. 1b), which was not elucidated by metal-centered quantum confinement mechanism since the intensity and the position of the adsorption bands only comes from the size effect of metal NCs, instead of a solvent effect. What attracts our particular interest is the emergence of paired excitation bands for both samples based on the measurement of excitation spectroscopy (Fig. 1a, c): Au NCs@GSH showed a broad excitation band of 330 nm with a shoulder peak at 375 nm (Fig. 1a, dotted lines), while the Au NCs@DT exhibited a blue-shifted and paired excitation at 280 nm with a shoulder peak at 325 nm (Fig. 1c, dotted line). Obviously, this solvent-induced PL enhancement cannot be only elucidated by free-electron confinement model[23].

The universal exhibition of paired excitation bands for each sample probably indicates that the one band with low energy is used as a dark or intermediate state to tune the emission of the triplet state with long lifetimes and high quantum yield. These observed optical transitions were previously assigned to the intraband and interband transitions of metal nanoclusters based on the size-dependent quantum confinement effect[23]. In contrast, our results demonstrated that the position and intensity of these optical absorptions and emissions are only dependent on the nature of the protecting ligands and the polarity of the solvents used, since the size of metal NCs before and after ligand exchange

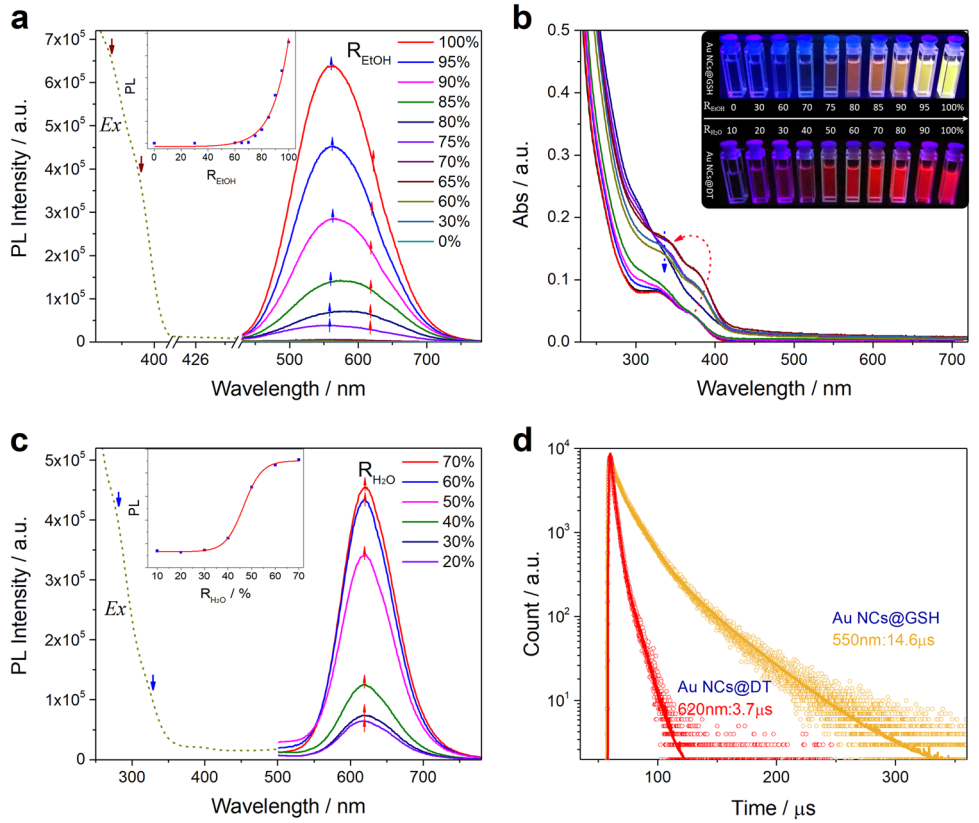

Fig. 1 Solvent-induced ligand-dependent optical absorption and emissions. Photoemission and excitation spectra of water-soluble Au NCs@GSH (**a**) and oil-soluble Au NCs@DT (**c**) in mixed solvents with different volume fraction *R* (Inset, relationship between the luminescence intensity and *R* ($R_{EtOH} = Vol_{EtOH} / Vol_{EtOH+H2O}$, $R_{H2O} = Vol_{H2O} / Vol_{EtOH+H2O}$), the spectra were recorded at 0.5 h after the sample preparation). **b** Ultraviolet-visible (UV−vis) absorption spectra of Au NCs@GSH in mixed solvents with different R_{EtOH}. Inset shows the digital photos of water-soluble Au NCs@GSH and oil-soluble Au NCs@DT in mixed solvents of ethanol and water with varied volume fraction R_{EtOH} and R_{H2O} under UV light. **d** Time-resolved luminescence decay profiles of solvent-induced luminescent Au NCs@GSH and Au NCs@DT

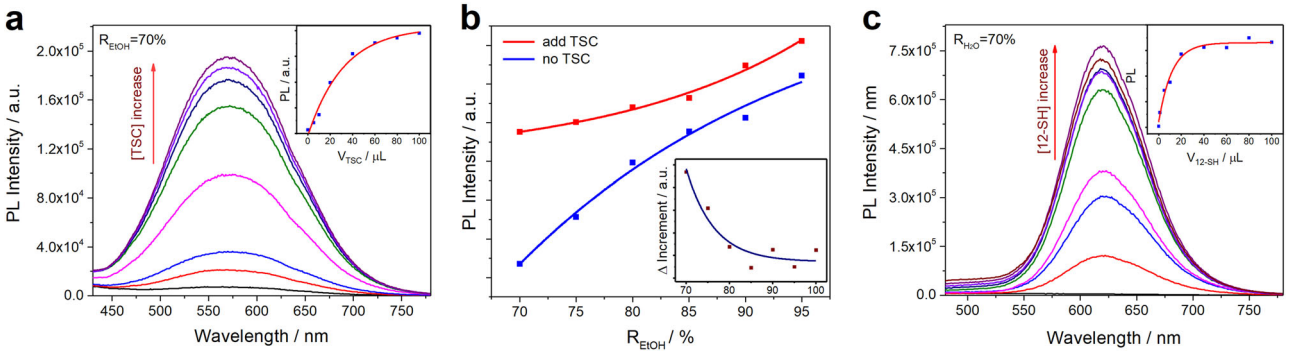

Fig. 2 PL enhancement of Au NCs. Introduction of organic molecules with targeted carbonyl and thiol functional groups. **a** Photoluminescence enhancement of Au NCs@GSH induced by addition of TSC into the Au NCs solutions in a volume fraction of ethanol (R_{EtOH}) of 70%. The inset displays the relationship between PL intensity and the added amount of TSC. **b** The photoluminescence enhancement of Au NCs@GSH by addition of equivalent TSC under different R_{EtOH}. **c** Photoluminescence enhancement of Au NCs@DT by addition of 1-dodecanethiol (DT) into the Au NCs solutions in a volume fraction of water (R_{H2O}) of 70%. The inset displays the relationship between PL intensity and the added amount of DT

is not changed. The contribution of the quantum state of metal clusters on the PL emission was overemphasized in the metal-centered quantum confinement model, while the critical role of surface ligand packing and assembly was seriously neglected.

The designed ligand adsorption experiment using organic molecules with targeted carbonyl and thiol functional groups, such as trisodium citrate (TSC) and 1-dodecanethiol, absolutely confirmed the paramount role of ligand assembly for tuning the photoluminescence emission of metal NCs. Noting that the kernel-composition of Au NCs was sustained after introducing carboxylate and thiolate, as verified by MALDI-TOF mass spectra (Supplementary Figs. 6 and 10). In Fig. 2a, with increasing amounts of TSC, the total PL intensity of Au NCs@GSH exponentially increases, and the increase of luminescence intensity mainly comes from the emission at ~550 nm due to the net increase of carbonyl groups (Supplementary Fig. 11), confirming our previously proposed interfacial clustering model[13]. The adsorption of more exotic carbonyl groups also

induces closer packing of thiol groups bearing on GSH on the metal core, simultaneously resulting in a medium intensity increase of emission at ~620 nm, even though the total number of thiol groups on the surface of Au nanocluster is constant. Very interestingly, we also found that the increment of PL enhancement was also strongly dependent on the initial solvent volume fraction of water to ethanol. At low R_{EtOH} values, the carboxyl ligands are loosely assembled on the metal core due to the competing adsorptions of carboxylate groups, with surface coordinated unsaturated metal atoms on the metal core, and water molecules by strong hydrogen bonding interactions in solution, which provide more available space for adsorption of the exotic TSC molecules. At high R_{EtOH} values, the close packing of carbonyl groups on the Au core has already formed by minimizing the hydrogen bonding between water and carboxyl functional groups to an extreme, preventing the adsorption of more TSC molecules (Fig. 2b and inset). Thus, with the increase of R_{EtOH}, the relative PL enhancement effect was not obvious. A similar PL enhancement effect following the same packing mode was also observed when 1-dodecanethiol was used as the dosing molecule (Fig. 2c). Thus, the dual emissions at 550 and 620 nm of individual Au NCs were unambiguously assigned to the carbonyl and thiol groups of the capping-ligands, respectively, and their adsorption and emission intensities strongly depend on the self-assembly of surface protecting ligands. However, here we cannot completely exclude generally accepted metal-centered surface ligand hybrid-electronic-state mechanism, such as LMMCT and LMCT models[9,11].

Ligand-directed assembly of preformed Cu NCs into highly anisotropic superlattices and related optoelectronic properties. To further emphasize the central role of ligand assembly on PL emission, the metal superlattice was designed to prove this key point. The metal superlattice (SL) usually refers to an ordered lower-dimensional structure, such as an array of quantum dots, dominated by weak interactions between amphiphilic molecules. As a control experiment, the Cu SL was fabricated by a self-assembling strategy using individual Cu nanoclusters as building units[24]. The main driving force for the formation of the Cu SL with a periodic structure is the strong hydrophobic interaction between the protecting DT molecules with a longer hydrocarbon chain. The delicate change of reaction conditions leads to the formation of highly anisotropic SL with varied morphologies, such as nanosheets in hexagonal packing and nanoribbons in lamellar phase, which were checked by transmission electron microscopy (TEM) and X-ray diffraction (XRD) (Fig. 3 and Supplementary Fig. 13). TEM images revealed that both the sheet- and ribbon-shaped SLs were composed of individual Cu NCs with identical sizes of ca. 2.0 nm (Fig. 3a, b and Supplementary Fig. 12).

The varied morphology of the SL is reminiscent of a self-assembling pattern of individual metal NCs, reflecting the interaction strength and the packing mode of the surface ligand DT in the SL, since the similarly sized Cu NCs were used as building units (Supplementary Fig. 14a). Obviously, according to the well-recognized metal-centered surface ligand hybrid-electronic-state model, the combination of the same hybrid states between the ligand and the metal should produce exactly the same luminous behavior, i.e., independent on the morphology of Cu SLs. The real case is exactly the opposite, and it shows a strong morphology-dependent PL emission: the nanoribbons exhibit a blue emission at 490 nm (Fig. 3e, blue line, and inset therein), while the nanosheet shows a red-shift green-yellow emission at ca. 550 nm (Fig. 3e, green line, and inset therein). These observations cannot be elucidated by classical free-electron model based on quantum confinement mechanism. By a close inspection, the only difference in the Cu SLs with varied morphology is the distance between two hydrophobic interacting DT molecules, as illustrated in Supplementary Fig. 14a: In the highly ordered structure (i.e., nanoribbon), due to the strong intercalation between DT molecules in the layers, the d-spacing between two DT molecules is larger than that in nanosheets, i.e., the overlapping or the interactions between paired or neighboring DT molecules are weak in the nanoribbons, which answers the blue-shift emission of the nanoribbons due to the declined electron delocalization between adjacent DT molecules.

Note that, when the well-ordered Cu SLs were ultrasonically disassembled into individual Cu NCs in ethanol, the strong luminescent emission was completely quenched (Fig. 3e, black line, and Supplementary Fig. 12c), consistent with results reported by Yang and coworkers[24]. However, when they were redispersed into water solvent, a distinguished red emission at 620 nm with a long lifetime and high QY (~5%) was recovered (Fig. 3e, red line and Supplementary Fig. 15), even the size, composition, and structure of individual Cu NCs remain intact; this was exactly same with DT-exchanged Au NCs in the above discussion (Fig. 1c), indicating that the PL emission of metal NCs is only dependent on the surface ligand self-assembling. In addition, according to the well-accepted metal-centered hybrid-state model, if the metal core is involved in the PL emission, different metals (Cu vs. Au) bonded by same surface ligands should have completely different PL emission behaviors. However, here, Cu NCs and Au NCs with the similar NP size surprisingly exhibited the same PL emissions with an identical wavelength of ca. 620 nm. Thus, the current experimental evidence strongly demonstrates that the hybrid orbital states of the metal are probably not involved in the electron excitation[9,25] i.e., the metal core does not play a decisive role to tune the adsorption and PL emission properties of metal NCs. Similar theory was proposed to understand the PL properties of Au NCs; however, the nature of localized electronic surface states was not well-investigated[16].

The distinguished changes of the UV−vis absorption and excitation spectra of the NCs during the assembling and disassembling of Cu SLs further confirmed the formation of an interface intermediate state resulting from the self-assembly of surface ligand molecules (Fig. 3e and Supplementary Fig. 16). Compared with Cu SLs, Cu NCs in water showed three strong absorption bands at 300, 330, and 380 nm, while individual Cu NCs in ethanol only exhibited a weak absorption at 330 nm, indicating that the formation of adsorption bands is strongly dependent on the assembly of surface ligands on the metal core[26,27]. The generation of adsorption bands that depend on the surface ligand assembly was also evidenced by the characterizations of the excitation spectra. Even though both the Cu nanosheet and nanoribbon SL exhibit two excitation bands at 310 and 360 nm, their relative intensity is different, resulting in different PL emission at varied wavelengths (Fig. 3e, blue and green color). When the SL is disassembled to individual Cu NCs in ethanol (good solvent), no excitation bands nor any consequent luminescence are shown, even though the DT molecules remain intact on the surface of the metal core; however, if they are redispersed into water (poor solvent), a paired excitation band at 280 nm with a shoulder at 330 nm is produced and is slightly blue-shifted compared to its SL counterparts (Fig. 3e, red color). This further proves that the bright photoluminescence of few-atom metal nanoclusters originates from the self-assembling of surface ligands, instead of the metal core. Therefore, we deduced that some new interface intermediate states originating from the surface ligand assembly were formed, which have a dynamic and quantized nature[13,26].

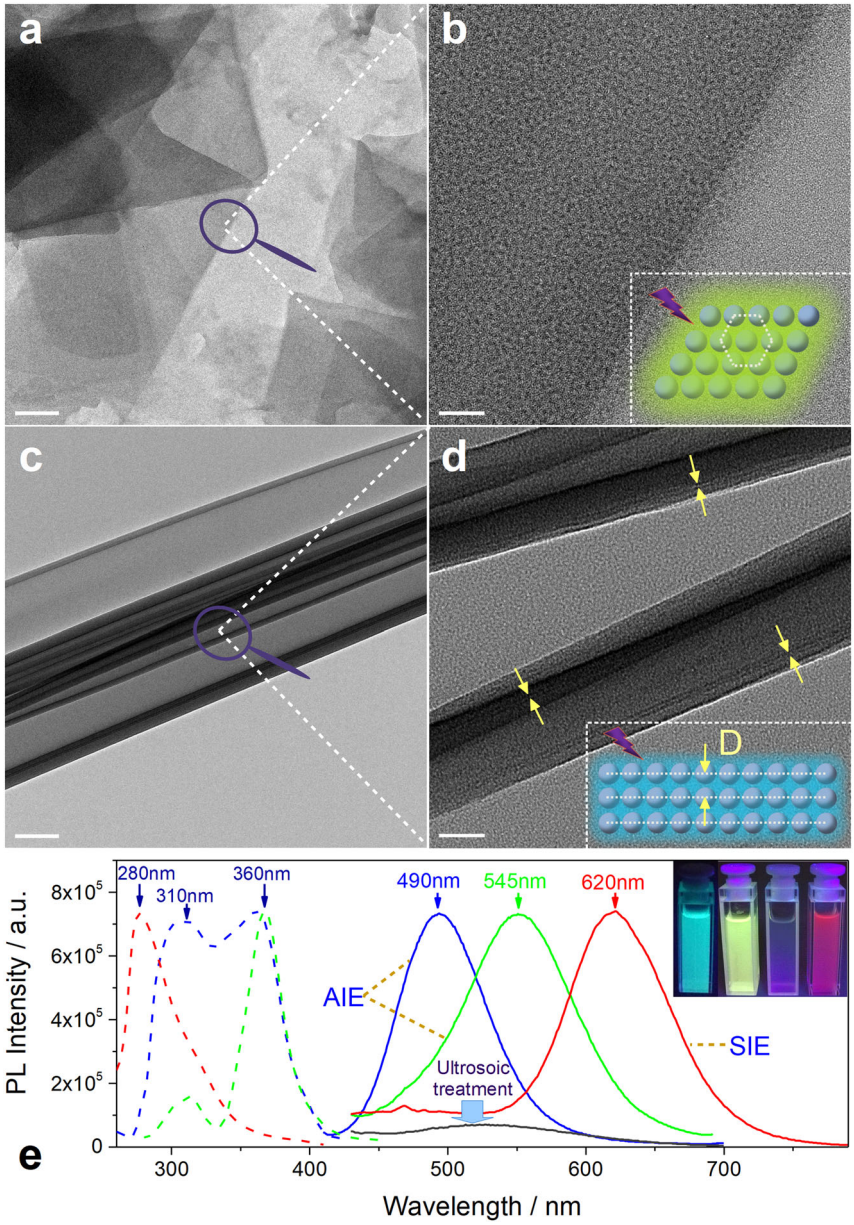

Fig. 3 Ligand-directed assembly of preformed Cu NCs. Highly anisotropic superlattices (SLs) and related optoelectronic properties. High-resolution transmission electron microscopy (HR-TEM) images of a Cu SL with a nanosheet structure (**a**, **b**) and a nanoribbon structure (**c**, **d**). The inset illustrations in **b** and **d** show the close packing mode of individual Cu NCs. (The scale bar in **a**, **c** and **b**, **d** is 200 and 20 nm, respectively.). **e** Excitation (dash) and emission spectra of Cu NCs SL with nanoribbon structure (blue), nanosheet structure (green), and individual Cu NCs in water (red). The insert shows the corresponding digital photos under UV light. AIE stands for the assembling-induced emission of the SL, and SIE is solvent-induced emission for individual metal NCs in a poor solvent

Ligand assembly in the confined nanopores of mesoporous silica nanospheres and tunable luminescent properties. To further prove the core role of surface ligands packing for tuning the PL of metal NCs, functional organosilanes with targeted carbonyl and amino groups in *3*-(triethoxysilyl)propylsuccinic anhydride and aminopropyl triethoxysilane, respectively, were covalently grafted on mesoporous silica (Fig. 4a, b)[28–30]. It should be mentioned that the functional group in the targeted organosilane contains electron-rich heteroatoms, such as oxygen (O) and nitrogen (N) with unpaired lone electrons, as with protective templates for the synthesis of metal NCs, such as unconjugated polymers containing carboxylate groups, proteins and amino acid molecules with nitrogen (N), oxygen (O), sulfur (S), phosphorus (P), and others. We observed that, even free of metal NCs, the amino-functionalized mesoporous silica nanoparticles (MSNs) showed a striking blue-light fluorescence emission at ca. 430 nm, and its excitation and emission spectra completely match, implying an AIE luminogen emission mechanism (Fig. 4c and Supplementary Fig. 17a).

Due to the variation of functional groups, the succinic-functionalized MSNs exhibited a remarkable red-color emission at ca. 615 nm with a short lifetime of 0.7 ns (Fig. 4d and Supplementary Fig. 17b). It is important to note that both single amino and succinic functional groups are nonluminescent. So far, to our best knowledge, this is the first example that simple organic functional-group-modified MSNs can emit a very strong

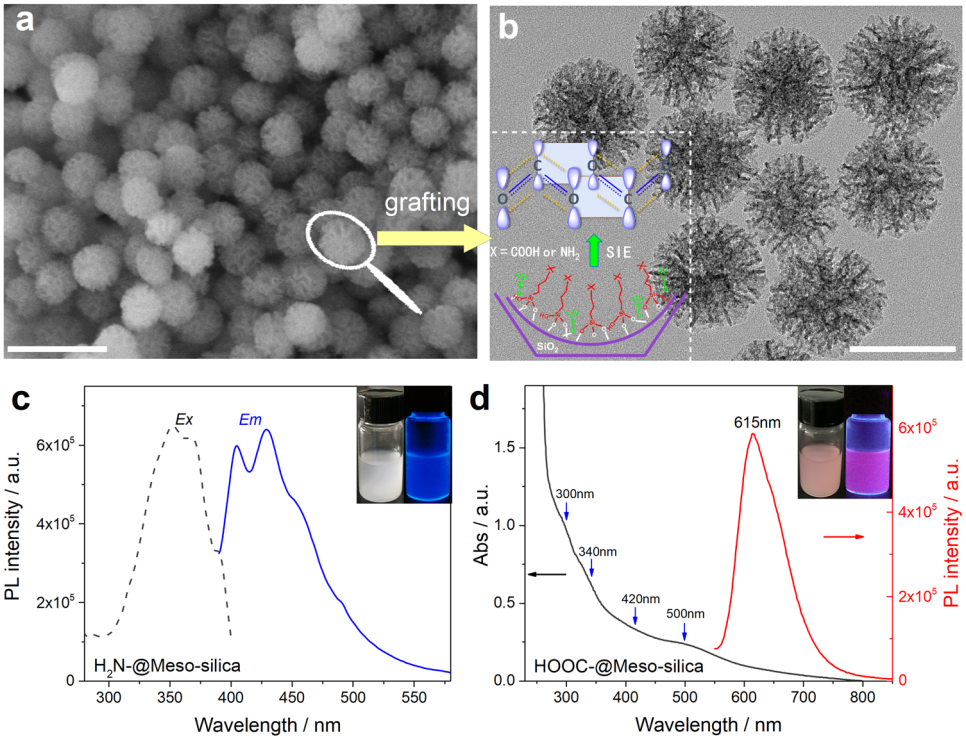

Fig. 4 Ligand assembly in the MSNs free of metals and their tunable luminescent properties. Scanning electron microscopy (SEM) (**a**) and TEM (**b**) images of as-synthesized fluorescent mesoporous silica nanoparticles. The inset shows the assembly of amino- and carbonyl- groups in the confined nanopores. (The scale bar in **a** and **b** is 200 and 100 nm, respectively.) **c** Excitation and emission spectra of aminopropyl-functionalized MSNs. **d** Absorption and emission spectra of propylsuccinic-functionalized MSNs

photoluminescence by the self-assembly of targeted molecules with electron-rich heteroatoms in the confined nanopores. In our previously reported results[28–30], we showed that currently used MSNs have unique spherical pores that are ca.3.0 nm in size (Fig. 4a, b), which greatly promote the self-assembling of organic functional groups in the confined space[31]. Generally, the excited transition of a single amino and carbonyl group in a range of 300–500 nm cannot be distinguished in the UV adsorption spectrum. It is reasonable that, in the confined nanospace of MSNs, the self-assembling of the amino and carboxylate groups, through space electronic interactions, namely, overlapping of the p orbital of lone pair (n) electrons among amino and carbonyl groups, extends the conjugation; thus, the corresponding intense and multiple adsorption bands in a range of 300–500 nm are observed with subsequent photoluminescent emissions (Fig. 4c, d).

However, the weak interaction between the organic functional groups with short flexible carbon chains makes it difficult to restrict the molecular vibration and rotation of amino and carbonyl groups in the pores, increasing the occurrences of nonradiative relaxation of the excited states. Therefore, only a moderate-intensity PL emission of organic grafted fluorescent MSNs was observed compared to the strong PL emission of metal NCs where the metal nanocluster core provides a series of high-symmetry, strong adsorption sites for surface capping-ligands through N/O/S/P−metal hybrid bonding, thus suppressing molecular vibration and rotation and enhancing the emission intensity of metal NCs, implying the anchoring role of metal core to the surface ligands. Even though the life times and QY of both systems are significantly different, the PL emission follows the same p-band-controlled model. We first demonstrated that the self-assembly of organic functions in these nanopores produced a stable and bright AIE-type luminogen as an emitter for PL emission (Fig. 4b, insert).

Ligand-assembly-mediated p-band intermediate state dominates photoluminescence emission. A common feature involves using protecting ligand molecules for the synthesis of metal NCs containing electron-rich heteroatoms, including oxygen (O), nitrogen (N), sulfur (S), and phosphorus (P), which often promotes the production of triplet excitons through n–π* transition and, hence, facilitates the spin-forbidden transfer of singlet-to-triplet excited states through intersystem crossing to populate triplet excitons[32,33]. A descriptive ligand-assembly-mediated interfacial PBIS model was proposed to understand the origin of the PL emission of metal NCs in Fig. 5. At the nanoscale interface of the metal nanocluster core or in the confined nanopores, the adjacent ligands locally interact with each other to form Rydberg matter-like clusters by the overlapping of p-orbitals from O, N, S, and P on proximal carbonyl/thiol groups with high-energy lone-pair electrons[34,35]. The delocalization of the high-energy electrons in coupled p orbitals in ligand-directed molecular architectures produces a new overall lower energy state, the so-called PBIS, which acts as an intermediate (or dark) state to tune PL emissions by intersystem crossing where the energy gap between the singlet excited state and the intermediate p-band state governs the direction and the extent of the electron transfer. This also answers why the excitation bands for each sample are always present in pairs.

To gain insight into the nature of the PBIS of metal clusters, we performed theoretical calculations on their electronic structures and energy levels by using the density functional theory (DFT) and time-dependent density functional theory (TD-DFT) methods at the cam-B3LYP/[aug-cc-pVTZ/6-311 + G(d, p) + SDD] level. Aug-cc-pVTZ was used for S atom and 6-311 + G(d, p) was employed for other nonmetal atoms. SDD was used for Au atom. Solvation effect was modeled by IEFPCM in water solvent. To simplify the calculation, the carbon chain (DT) was replaced by

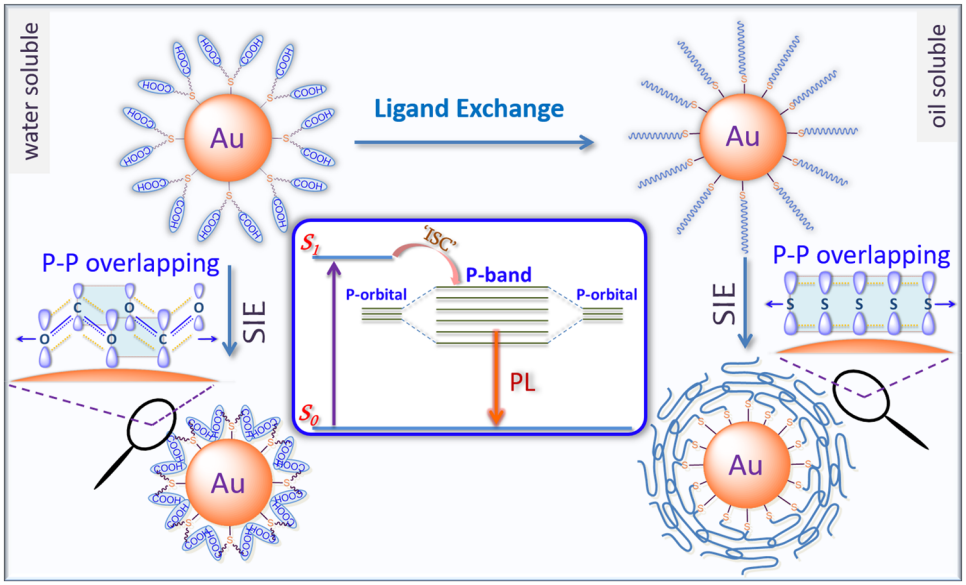

Fig. 5 Ligand-assembly-mediated PBIS dominates photoluminescence emission. Schematic illustration of the ligand exchange process and solvent-induced emission (SIE) properties of Au NCs (inset: the energy-level structure of Au NCs in water and ethanol mixed solution). The p-band formed by the overlapping of p-orbitals of electron-rich sulfur and oxygen heteroatoms of well-organized surface ligands is used as an intermediate state or dark state to tune the optoelectronic properties)

ethane (CH_3CH_2-SH) during the computational process and three molecular configurations (C_2H_5-SH, C_2H_5-S^- and C_2H_5-S-Au) were calculated to check the optimal electron structure for PBIS. As shown in Supplementary Fig. 18, these three mercapto monomer exhibit distinct molecular absorptions at UV region (<250 nm). The optimized conformations of the deprotonated molecule (C_2H_5-S^-) and their molecular orbital surfaces of HOMO and LUMO indicated that p orbitals of S element, i.e., S (p) make a significant contribution to the whole molecular orbital with a new adsorption band at 275 nm, as shown in Supplementary Fig. 18(c & d) and Supplementary Table 2. Differing from the monomers, their dimeric counterparts exhibit the completely different optoelectronic properties, which are very sensitive to the local proximity ligand chromophores, i.e., the distance of adjacent sulfur groups, in particular for (C_2H_5-S^-)$_2$ dimers (Fig. 6). As shown in Fig. 6a, for (C_2H_5-S^-)$_2$ dimers, it shows three sharp adsorption bands centered with wavelength larger than 270 nm, in perfect agreement to the assignments of adsorption bands of metal NCs (Fig. 1b), Cu superlattice (Fig. 3e) and ligand functionalized MSNs (Fig. 4c, d), and very interesting, with the decreasing of the S-S distance, the absorption peak with minimum energy gradually red shifted from 310 to 550 nm (Fig. 6a). By analyzing the composition of HOMO and LUMO orbitals, we find that the p-orbital of two S atoms were highly overlapped in HOMO orbital and the S(p) orbital makes a significant contribution to the whole molecular orbital (89.6%, Fig. 6b, inset), while the electron in LUMO orbital was dispersive and almost unaffected by the variation of S−S distance, which answers the red shift of absorption bands in Fig. 6a, b, and Supplementary Table 3. However, if we just consider the LMCT or LMMCT contribution of S-Au, the red shift of only single adsorption band at ca. 250 nm was not obvious (Fig. 6c, d, Supplementary Table 3). The presence of adsorption bands at the visible region, also probably answers PL emissions at the near-IR region[36,37]. When the CH_3CH_2-SH is coordinated with Au, the formation of S-Au hybrid orbital could easily observe whatever for monomers or dimers (Supplementary Figs. 18g, h, 19g, h, Supplementary Tables 2 and 3), whose HOMO-LUMO transition has a CT-like character of excitation from S-ligand to gold (in good agreement with an LMCT character). However, the main contribution of HOMO-LUMO transitions for PL comes from the intermidate P band state formed due to the overlapping of p orbitals of S atoms on the surface of metal NC (Fig. 6c, d, and Supplementary Table 3). Comparing these two charge density difference maps of C_2H_5-S-Au monomer and dimer, we also propose an alternative electron relaxation pathway to elucidate the PL emission origin of metal NCs due to the space interaction of heteroatom orbitals with the help of LMCT mechanism at the heterogeneous nanoscale interface: the first singlet transition was initiated from S-Au LMCT excitation, while the bonding strength of S-Au was weakened due to the p orbital overlapping of paired S atoms, and at ultrafast time scale, the excited electron was moved to the transient p-band intermediate state, and subsequent electron relaxation leads to the bright PL emission of metal NCs. The key point of this mechanism is the interfacial orbital redistribution through space interactions by fast switching between S-Au bond and intermediate p-band formed by orbital overlapping of paired S atoms. We believed that this mechanism provides a reliable physical elucidation for the classical Sabatier principle defining the best catalyst for a given reaction by precisely tuning the surface bonding strength[38]. Even though LMCT mechanism involved the relaxation of excited state, a main contribution for the PL comes from the transient intermediate p-band state due to the overlapping of p orbitals of S atoms on the surface of metal NC. These theory simulation results further verified that the p-orbital of heteroatom (N, O, S, P) could overlap efficiently when two heteroatoms were in a proper distance which could lead to the delocalization of electrons between neighboring heteroatoms accounts for its unique ligand-dependent PL properties. The more detailed study on the kinetic of PBIS states by transient absorption spectrum was under investigation.

The PBIS mechanism is completely different from the well-known single site surface trap state, where impurities are explained as the source of PL emission of heteroatom-doped semiconductors and carbon (or graphene) QDs[39]. The basic features of electronic structures of surface ligand p-bands are their energy bands resulting from the extended overlaps of atomic orbitals at the nanoscale. The energy level and width of a p-band

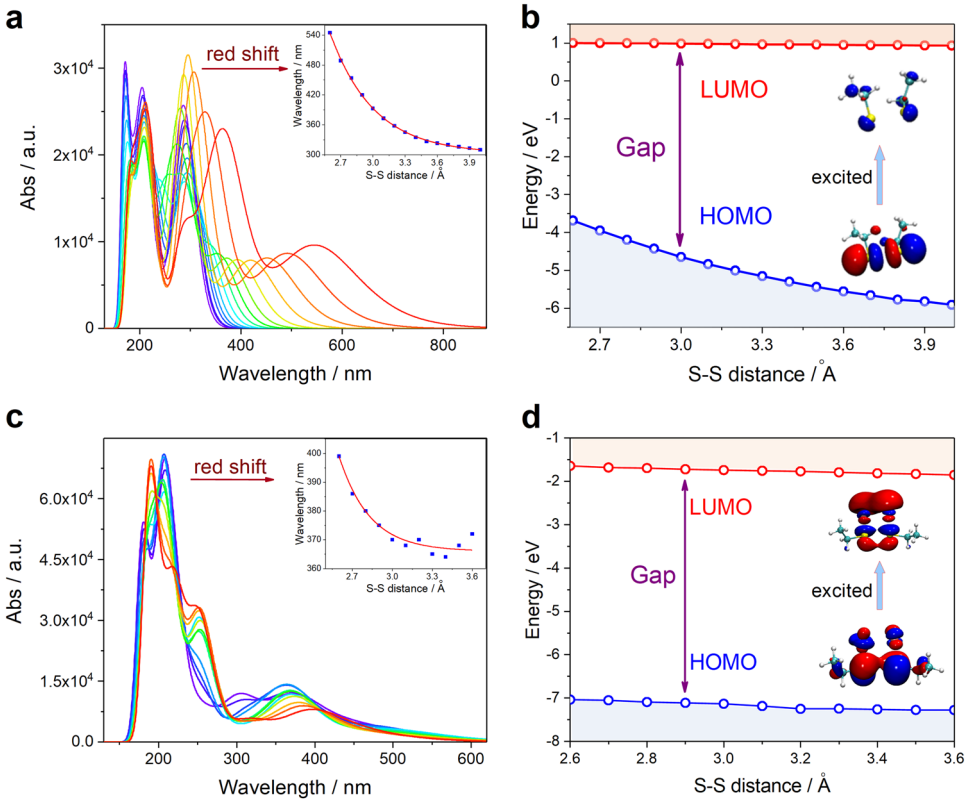

Fig. 6 Time-dependent density functional theory calculations. bi-C_2H_5-S^-, bi- bi-C_2H_5-S-Au with the variation of S—S distance. **a**, **c** The calculated absorption spectrum; the inset shows the variation of absorption peak with S—S distance. **b**, **d** DFT calculation results of HOMO (blue) and LUMO (red) energy levels of the conformations with various S—S distance. The typical excited transition from occupied orbital to unoccupied orbital is also illustrated

correlates to the delocalization degrees of its combinational atomic orbitals (AOs). In general, more delocalized AOs lead to wider energy bands with lower energy and vice versa. Indeed, our surface ligand p-band model shares a common physical nature with the interaction of orbitals through space in one molecule with several nonconjugated functional groups or chromophores first proposed by Hoffmann[40], whose orbitals or groups of orbitals, localized to a group, perhaps delocalized within that group, confer on that functional group its characteristic physical and chemical properties. But, our ubiquitous feature of our PBIS model reveals the intermolecular interactions of orbitals through space in confined nanospace or nanoscale interface with several nonconjugated functional groups or chromophores. The matching of energies between the excited states finally governs the direction and the extent of the electron transfer and its unique PL emissions (inset of Fig. 5).

Based on the PBIS model, the long-term debated and self-contradictory size-dependent and size-independent PL phenomena of Au NCs can be readily understood: the smaller the metal nanoparticle size, the more coordinated unsaturated metal atoms are exposed with increased surface-to-volume rations, resulting in strong binding and high surface coverage of surface coating ligands, and, consequently emitting enhanced PL intensity with low energy due to maximum overlapping of p orbitals from surface ligands. When the nanoparticle size is fixed, the intensity and wavelength of PL are dependent on ligand coverage or densities: a high Au-S coordination number (CN) and a high surface coverage results in stronger PL emission at long-wavelength because of the close packing of surface ligands, whereas a low Au-S CN and a low surface coverage make weak PL emission with high energy. This clearly answers why the thiolated PEGylated Au nanoparticles (NPs) exhibited a weaker PL emission at ca. 810 nm with lower energy[41], compared to GSH or DT protected Au NCs in our case. Obviously the thiolated PEG (PEG-SH) ligands with large molecular weight (MW) influenced the Au-S coordination number (CN) and surface coverage by steric effect. In fact, the observed aurophilic Au···Au interaction with neighboring sulfur atoms on the NLO efficiency of Au NCs was not conflict to our ligand-center PBIS model, since the interaction strength of the aurophilic Au···Au subunits (or the distance between two Au···Au subunits) reflects the change of distance between two adsorbed thiolate groups (S···S atoms), which determines the overlapping degree of two p orbitals of S atoms[42]. Obviously, our PBIS model clearly answers the aurophilic interaction on the NLO efficiency and the PL emission mechanism of transition organometallic complexes[43].

The multi-dispersity of PBIS with transient and quantized characteristics was also evidenced by UV—vis absorption and excitation spectra (Figs. 1a—c, 4c, d, and Supplementary Fig. 9). The presence of PBIS with different energy levels explained not only the origin of multichannel emissions of metal NCs, but also the long lifetime and high quantum yield of the PL emission of metal NCs. In addition, the rarely observed kinetics of the ligand exchange reaction and relaxation dynamic of excited states induced by a interplay of various noncovalent interactions revealed that the p-band formed by the strong coupling between the p orbitals of heteroatoms had a semi-covalent bond character[34,35], strongly competing with other weak interactions at the nanoscale interface, such as hydrogen bonding, $n \rightarrow \pi^*$ interactions, $\pi \rightarrow \pi$ stacking, and van der Waals interaction in solution[13,44–48]. In view of the paramount importance of ligand and interface interaction in nanocatalysis[3,18–22,49], the P-band theory could be a physical basis for elucidating the classical Sabatier principle defining the best catalyst for a given reaction,

where the optimum "bond strength" between reactant and catalytic active site could be tuned due to the presence of space interaction of orbitals from interfacial adsorbed species, including reactants, surface ligands, promoters (for example, the alkali-earth metal ions) and even water molecules around the active sites[38], and also the new p-band center provides an extra reaction channel to release the activation energy in a catalytic reaction by strong space interaction between the orbitals of reactants (in enzyme catalysis, it could be the interaction between substrate and amino acid residues or/and water molecules around the active site), not just considering the orbital hybridization between reactant and catalytic active site in the classical catalytic kinetics.

Using this model, our ligand- and solvent-dependent dual-colored phosphorescence emission of water-soluble and oil-soluble Au NCs at 550 and 620 nm was readily characterized by the presence and subsequent self-assembly of dual carbonyl and thiol functional groups bearing on the protecting ligand molecules. Usually, the phosphorescence produced by ISC transitions was not easily observed in fluid solutions at room temperature due to the enormous nonradiative deactivation processes during the long relaxation time, such as thermal and solvent relaxation. However, when surface-ligand-protected metal NCs were dispersed in the poor solvent or self-assembled in both the superlattice and the confined nanopores, the assembly of ligand binding sites perfectly protected surface excited states from collisional quenching, resulting in enhanced PL emission with high QY. Considering the diversity of the ligand binding motif and packing mode on the varied crystallographic planes of metal NCs[6,7,50–52], the previously reported abnormal luminescence phenomena for metal NCs now can be readily understood due to the formation of diversity of PBIS at the nanoscale interface, such as solvent-induced dual-luminescence emissions, large Stokes shift (near-infrared emission), high quantum yield, long lifetime emission, broad emission peak, and ligand selectivity. We believe that this significant conceptual advance is not only useful for explaining the peculiar optoelectronic properties of semi-conductor quantum dots, carbon (or graphene) quantum dots and MOFs[1–4,49,53–56], but also provides completely new insights for the understanding of multiexcitonic relaxation of singlet fission and photoluminescent organometallic complexes[43,47,57–59].

Discussion

Manipulating the delicate surface ligand interactions at the nanoscale interface of single a metal nanocluster, the superlattice, and mesoporous materials, we found that the resulting interplay of various noncovalent interactions leads to the precise modulation of emission colors and quantum yield. Our experiments demonstrate that the bright photoluminescence of few-atom metal nanoclusters originates from the self-assembling of surface ligands. This provides direct evidence for the effectiveness and rationality of a p-band-dominant ligand-centered model relative to the well-accepted metal-centered free-electron model. In addition, the calculations of TD-DFT even just for excited dimers (excimers) show the rationality of P-band model. The energy level of the p-band center formed through space interaction (or overlapping) of orbitals is very sensitive to the local proximity ligand chromophores at confined nanospace or nano-interface, i.e., the distance of neighboring groups. The dynamic PBIS, with diverse electronic band structures, exhibits unique transient and intermediate state characteristics to tune the direction and the extent of the electron transfer. This explains long-standing experimental puzzles on the abnormal PL emission features of metal NCs. Herein, as a candidate of light-emitting material for display devices, white light-emitting diodes (LEDs) with excellent illuminating capacity were home-fabricated by simply mixing three kinds of currently synthesized metal NCs with tunable blue-green, green, and red emissions (Supplementary Fig. 21, 22 and Supplementary Table 4). With respect to the importance and universality of the ligand and interface interaction, this PBIS conceptual advance not only elucidates the fundamental physical principles driving nanoscale PL emission phenomena, but also provides insights to understand the interfacial nanocatalysis (size and crystal facet effect), enzyme catalysis and the tailored biological functions by pre-ligand assembly in living cells on the molecule level.

Methods

TD-DFT calculations. To gain insight into the nature of the PBIS of metal clusters, we performed theoretical calculations on their electronic structures and energy levels by using the density functional theory (DFT) and time-dependent density functional theory (TD-DFT) methods at the cam-B3LYP[60]/[aug-cc-Pvtz[61,62] /6-311 + G(d, p)[63–65] + SDD[66,67]] level. Aug-cc-pVTZ was used for S atom and 6-311 + G(d, p) was employed for other nonmetal atoms. SDD was used for Au atom. Solvation effect was modeled by IEFPCM[68] in water solvent. To simplify the calculation, the carbon chain (DT) was replaced by ethane (CH_3CH_2-SH) during the computational process and four molecular configurations (C_2H_5-SH, C_2H_5-S^-, C_2H_5-S-Au…H_2O and C_2H_5-S-Au) with mono- and bimolecular structures were calculated to check the optimal electron structure for PBIS. For bimolecular systems, the geometries were optimized with S−S distance fixed from 2.6 to 4.0 Å, at intervals of 0.1 Å. In C_2H_5-S-Au…H_2O and (C_2H_5-S-Au…H_2O)$_2$, H_2O molecules were used to stabilize Au center as water was employed as solvent. All calculations were performed using the Gaussian09 program package[69] and molecular structure figures were prepared using CYLView[70].

Data availability

The data sets generated and analyzed during the current study are included in the Supplementary Information.

Received: 7 April 2019; Accepted: 24 October 2019;
Published online: 15 November 2019

References

1. Peyser, L. A., Vinson, A. E., Bartko, A. P. & Dickson, R. M. Photoactivated fluorescence from individual silver nanoclusters. *Science* **291**, 103–106 (2001).
2. Zheng, J., Nicovich, P. R. & Dickson, R. M. Highly fluorescent noble-metal quantum dots. *Annu. Rev. Phys. Chem.* **58**, 409–431 (2007).
3. Boles, M. A., Ling, D., Hyeon, T. & Talapin, D. V. The surface science of nanocrystals. *Nat. Mater.* **15**, 141–153 (2016).
4. Baker, S. N. & Baker, G. A. Luminescent carbon nanodots: emergent nanolights. *Angew. Chem. Int. Ed.* **49**, 6726–6744 (2010).
5. Luo, Z. et al. From aggregation-induced emission of Au(I)-thiolate complexes to ultrabright Au(0)@Au(I)-thiolate core-shell nanoclusters. *J. Am. Chem. Soc.* **134**, 16662–16670 (2012).
6. Zeng, C., Chen, Y., Kirschbaum, K., Lambright, K. J. & Jin, R. Emergence of hierarchical structural complexities in nanoparticles and their assembly. *Science* **354**, 1580–1584 (2016).
7. Jadzinsky, P. D., Calero, G., Ackerson, C. J., Bushnell, D. A. & Kornberg, R. D. Structure of a thiol monolayer-protected gold nanoparticle at 1.1 Å resolution. *Science* **318**, 430–433 (2007).
8. Walter, M. et al. A unified view of ligand-protected gold clusters as superatom complexes. *Proc. Natl. Acad. Sci. USA* **105**, 9157–9162 (2008).
9. Liu, J. et al. Luminescent gold nanoparticles with size-independent emission. *Angew. Chem. Int. Ed.* **55**, 8894–8898 (2016).
10. Wu, Z. & Jin, R. On the ligand's role in the fluorescence of gold nanoclusters. *Nano Lett.* **10**, 2568–2573 (2010).
11. Zheng, J., Zhou, C., Yu, M. & Liu, J. Different sized luminescent gold nanoparticles. *Nanoscale* **4**, 4073–4083 (2012).
12. Chen, Y. et al. Photoemission mechanism of water-soluble silver nanoclusters: ligand-to-metal-metal charge transfer vs strong coupling between surface plasmon and emitters. *J. Am. Chem. Soc.* **136**, 1686–1689 (2014).
13. Yang, T. et al. Interfacial clustering-triggered fluorescence-phosphorescence dual solvoluminescence of metal nanoclusters. *J. Phys. Chem. Lett.* **8**, 3980–3985 (2017).
14. Crawford, S. E. et al. Ligand-mediated "turn on," high quantum yield near-infrared emission in small gold nanoparticles. *J. Am. Chem. Soc.* **137**, 14423–14429 (2015).
15. Yi, C. et al. Ligand- and solvent-dependent electronic relaxation dynamics of Au25(SR)18– monolayer-protected clusters. *J. Phys. Chem. C* **121**, 24894–24902 (2017).

16. Wang, G., Huang, T., Murray, R. W., Menard, L. & Nuzzo, R. G. Near-IR luminescence of monolayer-protected metal clusters. *J. Am. Chem. Soc.* **127**, 812–813 (2015).
17. Yang, T. et al. Mechanism of photoluminescence in Ag nanoclusters: metal-centered emission versus synergistic effect in ligand-centered emission. *J. Phys. Chem. C* **123**, 18638–18645 (2019).
18. Cotnoir-White, D. et al. Monitoring ligand-dependent assembly of receptor ternary complexes in live cells by BRETFect. *Proc. Natl. Acad. Sci. USA* **115**, E2653–E2662 (2018).
19. Chan, F. K.-M. et al. A domain in TNF receptors that mediates ligand-independent receptor assembly and signaling. *Science* **288**, 2351–2354 (2000).
20. Maly, D. J., Choong, I. C. & Ellman, J. A. Combinatorial target-guided ligand assembly: identification of potent subtype-selective c-Src inhibitors. *Proc. Natl. Acad. Sci. USA* **97**, 2419–2424 (2000).
21. Deng, G. M., Zheng, L., Chan, F. K. & Lenardo, M. Amelioration of inflammatory arthritis by targeting the pre-ligand assembly domain of tumor necrosis factor receptors. *Nat. Med.* **11**, 1066–1072 (2005).
22. Esko, J. D. & Selleck, S. B. Order out of chaos: assembly of ligand binding sites in heparan sulfate. *Annu. Rev. Biochem.* **71**, 435–471 (2002).
23. Negishi, Y., Nobusada, K. & Tsukuda, T. Glutathione-protected gold clusters revisited: bridging the gap between gold(I)-thiolate complexes and thiolate-protected gold nanocrystals. *J. Am. Chem. Soc.* **127**, 5261–5270 (2005).
24. Wu, Z. et al. Assembly-induced enhancement of Cu nanoclusters luminescence with mechanochromic property. *J. Am. Chem. Soc.* **137**, 12906–12913 (2015).
25. Hammer, B. & Norskov, J. K. Why gold is the noblest of all the metals. *Nature* **376**, 238–240 (1995).
26. Sugiuchi, M. et al. Aggregation-induced fluorescence-to-phosphorescence switching of molecular gold clusters. *J. Am. Chem. Soc.* **139**, 17731–17734 (2017).
27. Ai, L. et al. Copper inter-nanoclusters distance-modulated chromism of self-assembly induced emission. *Nanoscale* **9**, 18845–18854 (2017).
28. Zhang, K. et al. Mononuclear-dinuclear equilibrium of grafted copper complexes confined in the nanochannels of MCM-41 silica. *Chem. Eur. J.* **17**, 14258–14266 (2011).
29. Zhang, K. et al. Facile large-scale synthesis of monodisperse mesoporous silica nanospheres with tunable pore structure. *J. Am. Chem. Soc.* **135**, 2427–2430 (2013).
30. Zhang, K. et al. Dendritic and core-shell-corona mesoporous sister nanospheres from polymer-surfactant-silica self-entanglement. *Chem. Eur. J.* **24**, 478–486 (2018).
31. Liu, P.-C. et al. A dual-templating strategy for the scale-up synthesis of dendritic mesoporous silica nanospheres. *Green Chem.* **19**, 5575–5581 (2017).
32. Zhao, J., Wu, W., Sun, J. & Guo, S. Triplet photosensitizers: from molecular design to applications. *Chem. Soc. Rev.* **42**, 5323–5351 (2013).
33. An, Z. et al. Stabilizing triplet excited states for ultralong organic phosphorescence. *Nat. Mater.* **14**, 685–690 (2015).
34. Campbell, E. K., Holz, M., Gerlich, D. & Maier, J. P. Laboratory confirmation of C60+ as the carrier of two diffuse interstellar bands. *Nature* **523**, 322–323 (2015).
35. Holmlid, L. The diffuse interstellar band carriers in interstellar space: all intense bands calculated from He doubly excited states embedded in Rydberg Matter. *Mon. Not. R. Astron. Soc.* **384**, 764–774 (2008).
36. Maity, S., Bain, D. & Patra, A. Engineering atomically precise copper nanoclusters with aggregation induced emission. *J. Phys. Chem. C* **123**, 2506–2515 (2019).
37. Kang, X. & Zhu, M. Tailoring the photoluminescence of atomically precise nanoclusters. *Chem. Soc. Rev.* **48**, 2422–2457 (2019).
38. Medford, A. J. et al. From the Sabatier principle to a predictive theory of transition-metal heterogeneous catalysis. *J. Catal.* **328**, 36–42 (2015).
39. Dong, Y. et al. Carbon-based dots co-doped with nitrogen and sulfur for high quantum yield and excitation-independent emission. *Angew. Chem. Int. Ed.* **125**, 7954–7958 (2013).
40. Hoffmann, R. Interaction of orbitals through space and through bonds. *Acc. Chem. Res.* **4**, 1–9 (1971).
41. Cho, H. S. et al. Tissue- and organ-selective biodistribution of NIR fluorescent quantum dots. *Nano Lett.* **9**, 2354–2359 (2009).
42. Bertorelle, F. et al. Au10(SG)10: a chiral gold catenane nanocluster with zero confined electrons. Optical properties and first-principles theoretical analysis. *J. Phys. Chem. Lett.* **8**, 1979–1985 (2017).
43. Yam, V. W., Au, V. K. & Leung, S. Y. Light-emitting self-assembled materials based on d8 and d10 transition metal complexes. *Chem. Rev.* **115**, 7589–7728 (2015).
44. Bartlett, G. J., Choudhary, A., Raines, R. T. & Woolfson, D. N. n→π* interactions in proteins. *Nat. Chem. Biol.* **6**, 615–620 (2010).
45. Crespo-Hernández, C. E., Cohen, B. & Kohler, B. Base stacking controls excited-state dynamics in A·T DNA. *Nature* **436**, 1141–1144 (2005).
46. Zhang, Y. et al. Visualizing coherent intermolecular dipole-dipole coupling in real space. *Nature* **531**, 623–627 (2016).
47. Scholes, G. D. et al. Using coherence to enhance function in chemical and biophysical systems. *Nature* **543**, 647–656 (2017).
48. León, I., Alonso, E. R., Cabezas, C., Mata, S. & Alonso, J. L. Unveiling the n→π* interactions in dipeptides. *Commun. Chem.* **2**, 3 (2019).
49. Kovalenko, M. V., Scheele, M. & Talapin, D. V. Colloidal nanocrystals with molecular metal chalcogenide surface ligands. *Science* **324**, 1417–1420 (2009).
50. Yang, H. et al. Ligand-stabilized Au13Cux (x = 2, 4, 8) bimetallic nanoclusters: ligand engineering to control the exposure of metal sites. *J. Am. Chem. Soc.* **135**, 9568–9571 (2013).
51. Zeng, C. et al. Total structure and electronic properties of the gold nanocrystal Au36(SR)24. *Angew. Chem. Int. Ed.* **124**, 13291–13295 (2012).
52. Voznyy, O., Dubowski, J. J., J. T. Yates, J. & Maksymovych, P. The role of gold adatoms and stereochemistry in self-assembly of methylthiolate on Au(111). *J. Am. Chem. Soc.* **131**, 12989–12993 (2009).
53. Becker, M. A. et al. Bright triplet excitons in caesium lead halide perovskites. *Nature* **553**, 189–193 (2018).
54. Huang, R. W. et al. Hypersensitive dual-function luminescence switching of a silver-chalcogenolate cluster-based metal-organic framework. *Nat. Chem.* **9**, 689–697 (2017).
55. Fisher, A. A. E., Osborne, M. A., Day, I. J. & Lucena Alcalde, G. Measurement of ligand coverage on cadmium selenide nanocrystals and its influence on dielectric dependent photoluminescence intermittency. *Commun. Chem.* **2**, 63 (2019).
56. Noblet, T. et al. Semiconductor quantum dots reveal dipolar coupling from exciton to ligand vibration. *Commun. Chem.* **1**, 76 (2018).
57. Smith, M. B. & Michl, J. Singlet fission. *Chem. Rev.* **110**, 6891–6936 (2010).
58. Rao, A. & Friend, R. H. Harnessing singlet exciton fission to break the Shockley–Queisser limit. *Nat. Rev. Mater.* **2**, 17063 (2017).
59. Wakasa, M., Yago, T., Sonoda, Y. & Katoh, R. Structure and dynamics of triplet-exciton pairs generated from singlet fission studied via magnetic field effects. *Commun. Chem.* **1**, 9 (2018).
60. Yanai, T., Tew, D. & Handy, N. A new hybrid exchange-correlation functional using the Coulomb-attenuating method (CAM-B3LYP). *Chem. Phys. Lett.* **393**, 51–57 (2004).
61. Kendall, R. A., Dunning, T. H. Jr. & Harrison, R. J. Electron affinities of the first-row atoms revisited. Systematic basis sets and wave functions. *J. Chem. Phys.* **96**, 6796–6806 (1992).
62. Woon, D. E. & Dunning, T. H. Jr. Gaussian-basis sets for use in correlated molecular calculations. III. The atoms aluminum through argon. *J. Chem. Phys.* **98**, 1358–1371 (1993).
63. Frisch, M. J., Pople, J. A. & Binkley, J. S. Self-consistent molecular orbital methods. 25. Supplementary functions for Gaussian basis sets. *J. Chem. Phys.* **80**, 3265–3269 (1984).
64. Clark, T., Chandrasekhar, J., Spitznagel, G. W. & Schleyer, P. V. R. Efficient diffuse function-augmented basis sets for anion calculations. III. The 3-21+G basis set for first-row elements, Li−F. *J. Comput. Chem.* **4**, 294–301 (1983).
65. Curtiss, L. A. et al. Extension of Gaussian-2 theory to molecules containing third-row atoms Ga-Kr. *J. Chem. Phys.* **103**, 6104–6113 (1995).
66. Fuentealba, P., Preuss, H., Stoll, H. & Vonszentpaly, L. A proper account of core-polarization with pseudopotentials: single valence-electron alkali compounds. *Chem. Phys. Lett.* **89**, 418–422 (1982).
67. Szentpály, L. V., Fuentealba, P., Preuss, H. & Stoll, H. Pseudopotential calculations on Rb+2, Cs+2, RbH+, CsH+ and the mixed alkali dimer ions. *Chem. Phys. Lett.* **93**, 555–559 (1982).
68. Scalmani, G. & Frisch, M. J. Continuous surface charge polarizable continuum models of solvation. I. General formalism. *J. Chem. Phys.* **132**, 114110 (2010).
69. Frisch, M. J. et al. *Gaussian 09, Revision D.01* (Gaussian, Inc., Wallingford, CT, 2009).
70. Legault, C. Y. *CYLview, 1.0b* (Université de Sherbrooke, Canada, 2009). http://www.cylview.org.

Acknowledgements

This work was supported by the NSFC (21573074, 21872053 and 21533002), the Science and Technology Commission of Shanghai Municipality (19520711400), the CAS key laboratory of Low-Coal Conversion Science & Engineering (KLLCCSE-201702) and the JORISS program, the Postdoctoral Science Foundation of China (2018M640360). K.Z. thanks ENS de Lyon for a temporary position as an invited professor in France.

Author contributions

T.Y. performed the main experiments. K.Z. conceived the experiments. K.Z and T.Y. designed the experiments. T.Y. is co-supervised by K.Z. and P.W. K.Z. and T.Y. proposed PBIS model and designed the figures for the manuscript with the assistance of P.W. F.H. performed the TD-DFT calculations and further optimized the PBIS model. K.Z. proposed the strong physical correlation of P-band center and the classical Sabatier principle, which will completely change people on the understanding of reaction nature of heterogeneous catalysis, nanocatalysis and even enzyme catalysis on the molecule level. T.Y. and S.Y. conducted the photoelectron spectroscopy experiments. B.S. and B.P.

conducted the SEM and TEM characterizations. E.Y. performed the synthesis of MSNs. T.Y., P.W. and K.Z. prepared the manuscript with contributions from all co-authors.

Competing interests

The authors declare no competing interests.

Additional information

Supplementary information is available for this paper at https://doi.org/10.1038/s42004-019-0233-1.

Correspondence and requests for materials should be addressed to F.H., P.W. or K.Z.

Reprints and permission information is available at http://www.nature.com/reprints

Publisher's note Springer Nature remains neutral with regard to jurisdictional claims in published maps and institutional affiliations.